

Square-lattice magnetism of diabolite $\text{Pb}_2\text{Cu}(\text{OH})_4\text{Cl}_2$

Alexander A. Tsirlin,^{1,2,*} Oleg Janson,² Stefan Lebernegg,² and Helge Rosner^{2,†}

¹*National Institute of Chemical Physics and Biophysics, 12618 Tallinn, Estonia*

²*Max Planck Institute for Chemical Physics of Solids, Nöthnitzer Str. 40, 01187 Dresden, Germany*

We report on the quasi-two-dimensional magnetism of the natural mineral diabolite $\text{Pb}_2\text{Cu}(\text{OH})_4\text{Cl}_2$ with a tetragonal crystal structure, which is closely related to that of the frustrated spin- $\frac{1}{2}$ magnet PbVO_3 . Magnetic susceptibility of diabolite is well described by a Heisenberg spin model on a diluted square lattice with the nearest-neighbor exchange of $J \simeq 35$ K and about 5 % of non-magnetic impurities. The dilution of the spin lattice reflects the formation of Cu vacancies that are tolerated by the crystal structure of diabolite. The weak coupling between the magnetic planes triggers the long-range antiferromagnetic order below $T_N \simeq 11$ K. No evidence of magnetic frustration is found. We also analyze the signatures of the long-range order in heat-capacity data, and discuss the capability of identifying magnetic transitions with heat-capacity measurements.

PACS numbers: 75.30.Et, 75.50.Ee, 75.10.Jm, 91.60.Pn

I. INTRODUCTION

Quantum spin systems show intricate low-temperature phenomena of fundamental^{1–4} and even applied^{5,6} interest. Despite strong quantum fluctuations that tend to impair and eventually destroy ordered spin states, most quantum magnets develop long-range magnetic order at sufficiently low temperatures. In two and three dimensions, the lack of the ordered state at zero temperature is only possible in frustrated magnets, where the competition between magnetic couplings amplifies quantum fluctuations. For example, systems of interest are those based on spin- $\frac{1}{2}$ in the square-lattice or kagomé-lattice geometries.³ The simple square lattice with nearest-neighbor Heisenberg interactions (J_1) is non-frustrated. However, a second-neighbor coupling J_2 frustrates the system and leads to a rich phase diagram of the $J_1 - J_2$ frustrated square lattice model that was extensively studied in the past.^{7–11}

Experimental search for the $J_1 - J_2$ systems on a square lattice remains a challenging problem. While materials with ferromagnetic (FM) J_1 can be prepared in a rather systematic fashion using the building blocks of V^{+4} phosphates,^{12,13} systems with antiferromagnetic (AFM) J_1 are less studied. In the limit of $J_2/J_1 \rightarrow 0$, Cu^{+2} -based coordination compounds^{14–17} and VOMoO_4 (Ref. 18) are excellent material prototypes of square-lattice systems with weak magnetic frustration. The stronger frustration with J_2/J_1 approaching 0.5 has been so far observed only in one material, PbVO_3 ($J_2/J_1 \simeq 0.35$), that remains controversial because muon spin rotation experiments detect the magnetic ordering below 43 K,¹⁹ but neither thermodynamic measurements nor neutron powder diffraction are capable of observing this magnetic transition.²⁰ Latest theoretical results suggest that above $J_2/J_1 = 0.35 - 0.4$ the $J_1 - J_2$ square-lattice system enters the spin-liquid regime, and the magnetic order vanishes.^{7,9–11} While PbVO_3 may lie on (or be close to) the boundary of this spin-liquid region, further systems with $J_2/J_1 \simeq 0.5$ are highly desirable.

The crystal structure of PbVO_3 is a tetragonal derivative of the perovskite type. The tetragonal distortion, which is essential for the quasi-two-dimensional (2D) square-lattice magnetism, is only rarely observed in perovskites. Similar structures are found in BiCoO_3 (Ref. 21) and in the “supertetragonal” polymorph of BiFeO_3 , which is stabilized in thin films.²² However, none of these compounds is suitable as a model system for the quantum spin- $\frac{1}{2}$ square-lattice model because both Co^{+3} and Fe^{+3} bear much higher and largely classical spins. Surprisingly, an appropriate structural analog of PbVO_3 can be found in a completely different family of materials. The Cu-based mineral diabolite, $\text{Pb}_2\text{Cu}(\text{OH})_4\text{Cl}_2$, has tetragonal crystal structure^{23,24} that can be derived from the perovskite structure type.

The structure of diabolite features isolated CuO_4 plaquettes that form magnetic layers in the ab plane. These layers are interleaved by Pb_2Cl_2 slabs (Fig. 1). The relation to the parent ABX_3 perovskite structure can be understood by writing the chemical composition of diabolite as $\text{Pb}_2(\text{Cu}\square)\text{X}_6$, where $\text{X} = \text{OH}, \text{Cl}$. This way, half of the B-type positions are vacant, with the resulting voids filled by the bulky OH^- anions. While this non-trivial transformation leaves little chemical similarity to perovskites, the crystal structure of diabolite still features the space group $P4mm$, same as in PbVO_3 and PbTiO_3 . This tetragonal crystal structure is perfectly suited for a quasi-2D magnetism, because the magnetic layers of Cu^{+2} atoms are well separated, with the shortest interlayer distance of 5.5 Å. The robust tetragonal symmetry entails the perfect square-lattice arrangement of the magnetic sites in the ab plane.

In the following, we present an experimental and computational study of diabolite. We show that this compound is indeed a good material prototype of the spin- $\frac{1}{2}$ square lattice. However, its J_2/J_1 ratio is very small, hence the magnetic frustration is weak. We discuss the origin of this low J_2 , and pinpoint another peculiarity, the dilution of the spin lattice through the formation of Cu vacancies that may have implications for experimental studies of the diluted square lattices with spin- $\frac{1}{2}$.

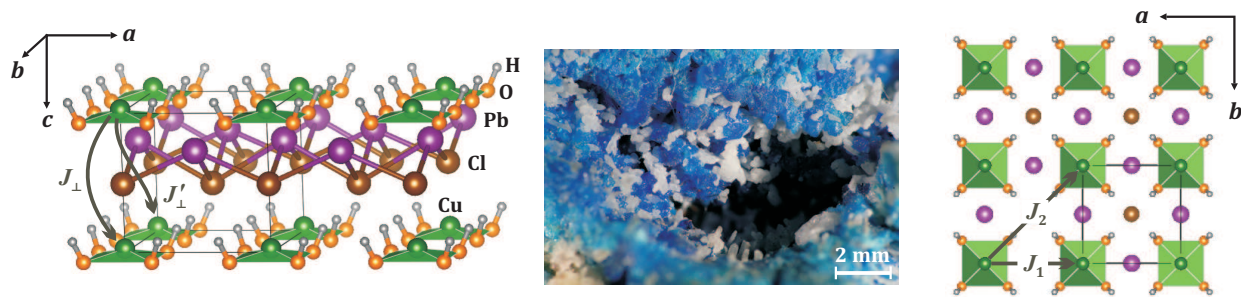


FIG. 1. (Color online) An overall view of the diabolite crystal structure (left panel) and its projection on the ab plane (right panel). Large spheres depict the Pb (violet) and Cl (brown) atoms located between the $[\text{Cu}(\text{OH})_4]$ magnetic layers. Green spheres inside the plaquettes are Cu atoms. Small spheres show the O (orange) and H (gray) atoms. The middle panel shows the natural sample of diabolite used in the present study. Note the translucent blue crystals of diabolite and opaque white crystals of laurionite and phosgenite (see Sec. II for details).

The outline of this paper is as follows. After summarizing experimental and computational methods in Sec. II, we report the detailed characterization of the natural mineral sample (Sec. III A) and elaborate on possible deviations from the ideal crystal structure (Sec. III B). We further develop microscopic magnetic models for both the ideal and distorted crystal structures (Sec. III C), and apply them to thermodynamic properties of diabolite (Sec. III D). Our results are discussed in Sec. IV, which is followed by a summary and an outlook.

II. METHODS

A natural sample of diabolite (Mammoth-Saint Antony Mine, Pinal Co., Arizona, USA) was provided by the mineralogical collection of the Department of Materials Research and Physics at Salzburg University. A visual inspection of this sample (Fig. 1, middle panel) identified translucent blue crystals of diabolite mixed with opaque white crystals of other minerals. Both blue and white crystals were detached from the support and separated manually. This way, a 100 mg batch of the diabolite crystals was obtained.

Phase composition of the samples was determined by laboratory x-ray diffraction (Huber G670 Guinier camera, $\text{CuK}\alpha_1$ radiation, ImagePlate detector, $2\theta = 3-100^\circ$ angle range). The batch of the blue crystals mostly contained diabolite, whereas white crystals were identified as a mixture of phosgenite ($\text{Pb}_2\text{Cl}_2\text{CO}_3$) and laurionite (PbOHCl). Considering possible contamination of the natural samples with variable – both crystalline and amorphous – impurities, sample quality was further checked by bulk chemical analysis and high-resolution x-ray diffraction (XRD). The chemical analysis was performed with the ICP-OES method.²⁵ The high-resolution XRD data were collected at the ID31 beamline of the European Synchrotron Radiation Facility (ESRF, Grenoble) at the wavelength of about 0.43 Å. Details of the experiment are described elsewhere.¹³ The Jana2006 program was used for the structure refinement.²⁶ Crystal struc-

tures were visualized using the VESTA software.²⁷

Magnetization measurements were performed with Quantum Design MPMS SQUID magnetometer in the temperature range 2 – 380 K in fields up to 5 T. Heat capacity was measured with Quantum Design PPMS in the temperature range 1.8 – 100 K in zero field and in the fields of 3 T, 6 T, and 9 T. All measurements were performed on polycrystalline samples.

Magnetic couplings in diabolite, as well as different aspects of its structural distortions, were analyzed by density-functional theory (DFT) band-structure calculations performed in the FPLO²⁸ and VASP²⁹ codes that implement basis sets of local orbitals and projected augmented waves,³⁰ respectively. Local density approximation (LDA)³¹ and generalized gradient approximation (GGA)³² for the exchange-correlation potential were used. Band-structure results are obtained for well-converged k meshes with 336 points in the symmetry-irreducible part of the first Brillouin zone for the crystallographic unit cell, and about 100 points for the supercells. Residual forces in optimized crystal structures were below 0.01 eV/Å. Effects of strong electronic correlations in the Cu 3d shell were treated by introducing the LDA band structure into an effective Hubbard model (model approach), or within the mean-field DFT+ U procedure, with the on-site Coulomb repulsion parameter $U_d = 6.5$ eV and the Hund's exchange parameter $J_d = 1$ eV applying the around-mean-field double-counting correction scheme.³³ Details of the computational procedure are described in Sec. III C.

Thermodynamic properties and Néel temperatures of the spin models relevant to diabolite were obtained from quantum Monte-Carlo (QMC) simulations based on the loop³⁴ and dirloop_sse³⁵ algorithms of the ALPS³⁶ simulation package. Simulations were performed on 2D ($L \times L$) and 3D ($L \times L \times L/5$) finite lattices with $L \leq 80$ and $L \leq 50$, respectively. Size convergence for the thermodynamic properties (magnetization and magnetic specific heat) was carefully checked. The magnetic ordering temperatures (T_N) were determined by calculating temperature dependence of the spin stiffness ρ_s for different

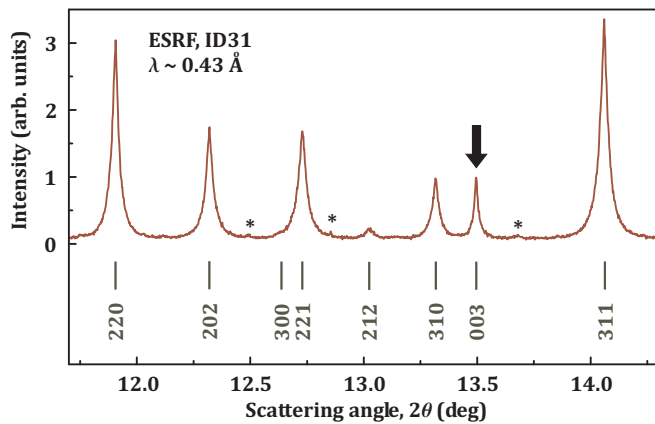


FIG. 2. (Color online) High-resolution XRD pattern of the natural sample of diabolite. Ticks show the reflection positions, whereas asterisks mark tiny reflections of the phosgenite impurity. The reflections of the second impurity, wherryite, are not visible in this angular range. Note that the 003 reflection is narrower than the reflections with non-zero h and/or k .

L and applying the appropriate scaling procedure, as previously described in Refs. 37 and 38.

III. RESULTS

A. Sample characterization

The high-resolution XRD pattern of the natural diabolite sample reveals strong reflections of the tetragonal diabolite phase along with few very weak reflections that are attributed to the impurities of phosgenite ($\text{Pb}_2\text{Cl}_2\text{CO}_3$) and wherryite [$\text{Pb}_7\text{Cu}_2(\text{SO}_4)_4(\text{SiO}_4)_2(\text{OH})_2$]. The amounts of these impurities are 1.1(1) wt.% and 0.4(1) wt.%, respectively, according to the Rietveld refinement.³⁹ While phosgenite is a diamagnet, no information on the magnetism of wherryite is presently available. Nevertheless, trace amounts of this impurity should not affect any of the results presented below.⁴⁰

Chemical analysis delivered the following bulk composition of the natural sample: 68.1(1) wt.% Pb, 9.3(1) wt.% Cu, and 0.2(1) wt.% Ba. Other elements amenable to the ICE-OES determination (including transition metals, but excluding O, H, and Cl) are below the detection limit of 0.1 wt.%. These estimates are in reasonable agreement with the expected chemical composition (67.2 wt.% Pb, 10.3 wt.% Cu), although slight deviations in the Pb and Cu content, as well as the presence of Ba, signal subtle variations in the stoichiometry of the diabolite phase.

The Rietveld refinement of the atomic positions resulted in reasonable atomic displacement parameters (ADPs) of Pb, Cl, and O, $U_{\text{iso}} \simeq 0.01 \text{ \AA}^2$ (the hydrogen position was not refined).³⁹ However, the notably higher ADP of Cu ($U_{\text{iso}} \simeq 0.035 \text{ \AA}^2$) suggested the miss-

ing scattering density at the Cu position. Considering the nearly isotropic thermal ellipsoid ($U_a^{\text{Cu}} \simeq 0.03 \text{ \AA}^2$, $U_c^{\text{Cu}} \simeq 0.04 \text{ \AA}^2$ along the a and c directions, respectively), the large ADP of Cu can not be explained by a displacement of Cu from its position on the four-fold axis, and should be rather understood as the formation of vacancies. Indeed, as the ADP was fixed to $U_{\text{iso}} = 0.01 \text{ \AA}^2$, the refined Cu occupancy converged to 0.942(4) indicating the deficiency of Cu atoms in the diabolite structure.⁴¹ The formation of Cu vacancies conforms to the underestimated Cu content from the chemical analysis that yields about 10 % Cu deficiency in the diabolite sample.

The formation of Cu vacancies is justified by both powder XRD and chemical analysis. Indeed, the missing scattering density in XRD could be otherwise explained by the substitution of a lighter element in the Cu position. However, the chemical analysis does not show detectable amounts of any foreign elements that are capable of replacing Cu in the diabolite structure. Trace amounts of Ba are likely related to the Pb/Ba substitution, which is favored by the similar ionic radii of these elements. The amount of the substituted Ba is well below 1 %, so it does not show up in the XRD refinement.

Another conspicuous feature of the natural diabolite sample is the sizable broadening of the hkl reflections with non-zero indices h and/or k . This effect is well seen in Fig. 2 where, for example, the 310 reflection is much broader than the neighboring 003 peak.³⁹ Anisotropic reflection broadening can be understood as the formation of stacking faults in the layered crystal structure of diabolite. This problem is further addressed in Sec. III B, where we also elaborate on the nature of Cu vacancies in the diabolite structure.

B. Details of the crystal structure

The structure refinement puts forward several issues regarding details of the atomic arrangement that may be important for understanding the magnetism of diabolite: i) positions of hydrogen atoms that are not precisely determined by XRD; ii) formation of Cu vacancies; iii) stacking faults that underlie the reflection broadening.

The position of hydrogen has been determined from single-crystal XRD²⁴ using the soft constraint on the O–H bonds (the O–H distance of 0.98 Å). We further refined the hydrogen position by a DFT-based structure optimization, with all atoms other than hydrogen fixed to their experimental positions. Both LDA and GGA optimizations⁴² converged to very similar results. The hydrogen atom is in the 4d position (x, x, z) with $x = 0.2975/0.2972$ and $z = 0.1191/0.1179$ in LDA/GGA, respectively. The resulting O–H distance is 0.99 Å, and the Cu–O–H angle is about 112.3°. These parameters only slightly differ from those found experimentally: the O–H distance of 0.98 Å (constrained) and the Cu–O–H angle of 109.1°.

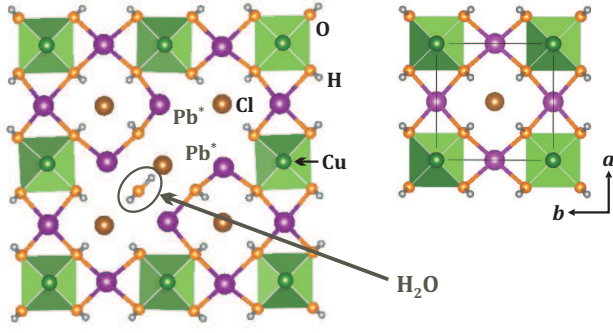


FIG. 3. (Color online) Left panel: formation of Cu vacancies in the magnetic layer of diaboleite ($\frac{1}{4}$ of Cu atoms and the respective amount of oxygens are removed). Top right panel: the pristine structure of stoichiometric diaboleite. The removal of one Cu and one O atom releases a water molecule. Additionally, the coordination of Pb atoms changes from four longer Pb-O bonds (2.45 Å, top right panel) to two shorter Pb*-O bonds (2.32 Å and 2.40 Å, respectively; left panel). Only the Pb-O bonds shorter than 2.5 Å are shown. The notation of atoms follows Fig. 1.

The formation of Cu vacancies can be explained as follows. The removal of one Cu atom creates an uncompensated negative charge that should be balanced by the removal of one oxygen or two chlorines. As the oxygen atoms are strongly bonded to Cu with the Cu-O distance of 1.97 Å, the removal of oxygen is expected. The remaining hydrogen atom may join one of the OH groups to form a water molecule. Regarding the four oxygen atoms that surround the vacancy, one is removed to compensate the charge, one oxygen forms the water molecule, whereas the two remaining OH groups are still bound to Pb. The resulting structure has been fully relaxed within GGA+ U to yield the configuration shown in Fig. 3 where we consider the 2×2 supercell with one out of four Cu atoms removed. This supercell with 25 % Cu deficiency should be representative for the actual diaboleite sample that features 5–10 % of Cu vacancies. The calculations for lower concentrations of vacancies would require even larger supercells, which are hardly feasible for an accurate computational treatment.

The formation of Cu vacancies enhances the Pb-O bonding and reduces the coordination number of Pb atoms around the vacancy. In stoichiometric diaboleite, each Pb atom is surrounded by four oxygens with the Pb-O separations of 2.45 Å. In Cu-deficient diaboleite, the Pb* atoms (Fig. 3) are strongly bound to only two O atoms, but the respective Pb-O distances are shortened to 2.32 Å and 2.40 Å, respectively. The bond to the third oxygen atom extends to 2.53 Å, whereas the fourth bond is either lost (for Pb* atoms adjacent to the oxygen vacancy) or stretched up to 2.63 Å (for the oxygen atom of the water molecule). This way, the lengths of the Pb-O bonds are redistributed, and bonding requirements of Pb can be satisfied, even though one out of four oxygen atoms is removed from the crystal structure. The

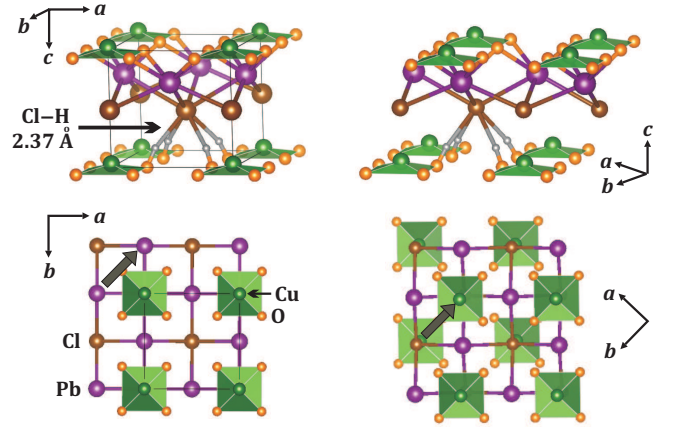
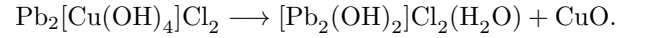


FIG. 4. (Color online) Possible mechanism of stacking faults in the diaboleite structure. The notation of atoms follows Fig. 1. Left panels: parent tetragonal crystal structure. Right panels: optimized structure with the uniform shift of the $[\text{Cu}(\text{OH})_4]$ layers for $\mathbf{k} = (\frac{1}{2}, \frac{1}{2}, 0)$. Note that the $[\text{Pb}_2\text{Cl}_2]$ slabs are invariant to this translation, which is denoted by the thick arrow. The weak $\text{Cl} \cdots \text{H}$ hydrogen bonds are the only interaction between the $[\text{Pb}_2\text{Cl}_2]$ slab and the neighboring $[\text{Cu}(\text{OH})_4]$ layer. Therefore, the structures with $\mathbf{k} = 0$ (left panel) and $\mathbf{k} = (\frac{1}{2}, \frac{1}{2}, 0)$ (right panel) marginally differ in energy. In the bottom panels, hydrogen atoms are omitted for clarity.

void formed between the two Pb* atoms (Fig. 3) is typical for Pb^{+2} oxides. It can be ascribed to the “localization” of $6s^2$ lone pairs that form a non-bonding region in the crystal structure.⁴³

The formation of Cu vacancies can be considered as the removal of CuO from the diaboleite structure. The local transformation is written as follows:



This formal equation reflects the fact that the complex anion $[\text{Cu}(\text{OH})_4]^{2-}$, with four OH groups attached to the Cu atom, is transformed into the complex cation $[\text{Pb}_2(\text{OH})_2]^{2+}$, where the two remaining OH groups are attached to Pb. To evaluate the energetics of Cu vacancies, we use a similar equation and replace the fictitious (and presumably unstable) $[\text{Pb}_2(\text{OH})_2]\text{Cl}_2(\text{H}_2\text{O})$ compound with the aforementioned metastable diaboleite having 25 % of Cu vacancies (Fig. 3). Using fully relaxed atomic configurations of this Cu-deficient diaboleite, pristine stoichiometric diaboleite, and CuO (tenorite),⁴⁴ we obtain the energy of +0.27 eV/f.u. (about 10 kJ/mol) for the formation of 25 % of Cu vacancies. Although rather large, this additional energy can be partially tolerated by the entropy term and by chemical potentials of different ions under specific growth conditions. Note that $\text{Pb}_2\text{Cu}(\text{OH})_4\text{Cl}_2$ is prepared in water solution⁴⁵ and likely follows a similar route of crystal growth in the natural environment.

Finally, we consider the problem of stacking disorder. The structure of diaboleite is formed by $[\text{Pb}_2\text{Cl}_2]$

slabs that are linked to the $[\text{Cu}(\text{OH})_4]$ units via the Pb–O bonds. On the opposite side of the slab, the connection to the next $[\text{Cu}(\text{OH})_4]$ magnetic layer is restricted to weak $\text{H}\cdots\text{Cl}$ hydrogen bonds (Fig. 4, top left panel). Each Cl atom is bonded to four hydrogen atoms of the neighboring unit, with the H–Cl distances as large as 2.37 Å. This value approaches the upper limit of O–H \cdots Cl distances reported in the literature.⁴⁶ The weak interlayer interaction enables regular shifts of the neighboring $[\text{Pb}_2\text{Cl}_2][\text{Cu}(\text{OH})_4]$ layers, and facilitates the stacking disorder.

In the tetragonal diabolite structure, the layers are stacked on top of each other (displacement vector $\mathbf{k} = 0$). An alternative stacking sequence could be based on $\mathbf{k} = (\frac{1}{2}\frac{1}{2}0)$ because the $[\text{Pb}_2\text{Cl}_2]$ slabs and even oxygen atoms are invariant to this translation, which only changes the order of Cu atoms and vacancies (note the $\text{Pb}_2\text{Cu}\square\text{X}_6$ formula discussed in Sec. I) along with hydrogen atoms. The resulting structure is monoclinic, with the twice larger unit cell and the Cm symmetry (Fig. 4). In GGA+ U , it lies only 40 meV/f.u. above the ideal tetragonal structure. This small energy difference is comparable to the entropy term and allows for the formation of stacking faults that are indeed observed experimentally.

To understand the effect of these stacking faults on the reflection broadening, we note that the stacking sequence with $\mathbf{k} = (\frac{1}{2}\frac{1}{2}0)$ leads to a monoclinic unit cell with the lattice vectors $\mathbf{a}' = \mathbf{a} + \mathbf{b}$, $\mathbf{b}' = \mathbf{a} - \mathbf{b}$, and $\mathbf{c}' = \frac{\mathbf{a}+\mathbf{b}}{2} + \mathbf{c}$, where \mathbf{a} , \mathbf{b} , and \mathbf{c} are lattice vectors of the parent tetragonal unit cell. The $a'b'$ plane of the monoclinic cell is fixed as the plane of the diabolite layer. However, the c' axis can have two different orientations, $\frac{\mathbf{a}+\mathbf{b}}{2} \pm \mathbf{c}$. Its position also depends on the precise value of the monoclinic angle between a' and c' . Therefore, in the reciprocal space the direction of the $(\mathbf{c}')^*$ axis is fixed $[(\mathbf{c}')^* \perp \mathbf{a}', \mathbf{b}', \text{i.e., } (\mathbf{c}')^* \parallel \mathbf{c}]$, whereas the direction of the $(\mathbf{a}')^*$ axis is variable. This explains why the $(00l)$ reflections remain narrow, although the reflections with large h and k substantially broaden. Indeed, the refinement of the anisotropic strain broadening yields the largest $hk0$ component, which is related to the variable position of the $(\mathbf{a}')^*$ axis.³⁹

Although our detailed study of the crystallographic issues is largely motivated by effects observed in the natural sample of diabolite, similar features are likely relevant to the $\text{Pb}_2\text{Cu}(\text{OH})_4\text{Cl}_2$ phase in general. The layered nature of the crystal structure facilitates the stacking disorder, whereas the formation of Cu vacancies can be instrumental in tuning low-temperature magnetism of this material. In the following, we report experimental data on thermodynamic properties of diabolite and analyze them from the microscopic viewpoint by considering the parent tetragonal crystal structure of stoichiometric diabolite along with possible deviations from this ideal atomic arrangement.

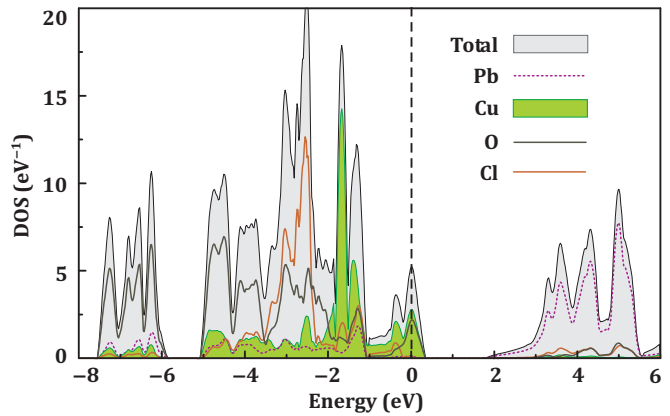


FIG. 5. (Color online) LDA density of states (DOS) for the stoichiometric diabolite. The Fermi level is at zero energy.

C. Microscopic magnetic model

The LDA energy spectrum of diabolite is typical for a cuprate compound. The valence band is dominated by oxygen 2p states, with sizable contributions of Cl 3p around -3 eV, and Cu 3d above -2 eV (Fig. 5). The large underestimate of strong electronic correlations leads to the spurious metallic energy spectrum in LDA. The LSDA+ U and GGA+ U calculations yield the band gap of about 2.7 eV in accord with the blue color of diabolite crystals (Fig. 1, middle panel).

The Fermi level is crossed by a single band (Fig. 6), which is of $d_{x^2-y^2}$ origin according to the conventional crystal-field levels of a strongly elongated octahedron (the in-plane Cu–O distances are 1.97 Å, whereas the out-of-plane Cu–Cl distances are 2.55 Å and 2.95 Å). The Cu $d_{x^2-y^2}$ band is well reproduced by a tight-binding model with the leading nearest-neighbor intraplane hopping $t_1 = 78$ meV and several long-range interactions that are all weak (Table I). Note that the coupling between the magnetic layers is provided by both t_\perp (along the c direction) and t'_\perp (along [101]). Other hoppings are below 2 meV and can be safely neglected in the minimal microscopic model.⁴⁷

Introducing the LDA hoppings into a Hubbard model with the effective on-site Coulomb repulsion $U_{\text{eff}} = 4.5$ eV,³³ we identify $\text{Pb}_2\text{Cu}(\text{OH})_4\text{Cl}_2$ as a magnetic insulator with $t/U_{\text{eff}} < 0.02$. Therefore, perturbation theory in t_i/U_{eff} enables the evaluation of AFM couplings as $J_i^{\text{AFM}} = 4t_i^2/U_{\text{eff}}$ to the lowest (second) order. We find $J_1^{\text{AFM}} = 63$ K and a very weak frustration by the second-neighbor coupling ($J_2^{\text{AFM}}/J_1^{\text{AFM}} < 0.01$). Weak interlayer couplings J_\perp and J'_\perp render diabolite a good quasi-2D magnetic system.

The above estimates are based on the model approach that yields the AFM couplings only. However, magnetic couplings – especially those that are short-range – may also include a FM component. This FM component can be taken into account by total-energy calculations (supercell approach) where energies of collinear spin states

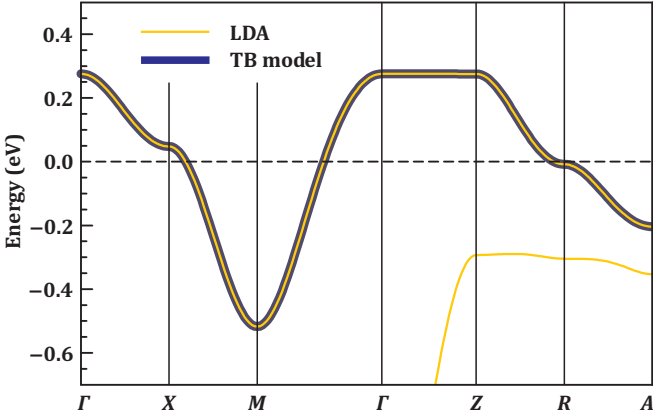


FIG. 6. (Color online) LDA band structure of stoichiometric tetragonal diabolite (thin light lines) and the fit with the tight-binding model for the Cu $d_{x^2-y^2}$ band (thick dark line). The k path is defined as follows: $\Gamma(0, 0, 0)$, $X(0.5, 0, 0)$, $M(0.5, 0.5, 0)$, $Z(0, 0, 0.5)$, $R(0.5, 0.5, 0.5)$, $A(0.5, 0, 0.5)$ in units of $2\pi/a$, $2\pi/b$, and $2\pi/c$, respectively.

TABLE I. Cu–Cu distances (in Å), transfer integrals t_i (in meV), and exchange couplings J_i (in K) in the tetragonal stoichiometric diabolite. The AFM components are obtained as $J_i^{\text{AFM}} = 4t_i^2/U_{\text{eff}}$ with $U_{\text{eff}} = 4.5$ eV, whereas the J_i values are calculated using the supercell approach. The superexchange pathways are shown in Figures 1 and 7.

	Cu–Cu distance	t_i	J_i^{AFM}	J_i
J_1	5.88	78	63	38
J_2	8.32	−7	0.5	0.5
J_{\perp}	5.50	−10	1.0	1.0
J'_{\perp}	8.05	9	0.8	0.4

are mapped onto the Heisenberg model to yield full exchange couplings J_i (Table I). Then the FM component is evaluated as $J_i^{\text{FM}} = J_i - J_i^{\text{AFM}}$. In the case of diabolite, this procedure only slightly changes the microscopic scenario. According to Table I, J_1 remains the leading interaction in diabolite, whereas other couplings are weak and AFM.

To elucidate the origin of magnetic couplings in diabolite, we calculated the Wannier functions (WF) based on the Cu $d_{x^2-y^2}$ orbital character. Each WF (Fig. 7) includes the Cu $d_{x^2-y^2}$ orbital along with the σp orbitals of oxygen atoms. The superexchange pathway of J_1 involves the 90° overlap of the neighboring WFs (Fig. 7), which generally leads to a FM contribution to the exchange.⁴⁸ Indeed, we find a sizable FM component $J_1^{\text{FM}} = J_1 - J_1^{\text{AFM}} = -25$ K (Table I). The second-neighbor coupling J_2 features a more favorable 180° pathway. However, the O–O distance of 4.43 Å is too large for an efficient overlap of the oxygen orbitals, and the resulting coupling is very weak.

Finally, we evaluate magnetic couplings for the stoichiometric diabolite with the displaced layers (Fig. 4)

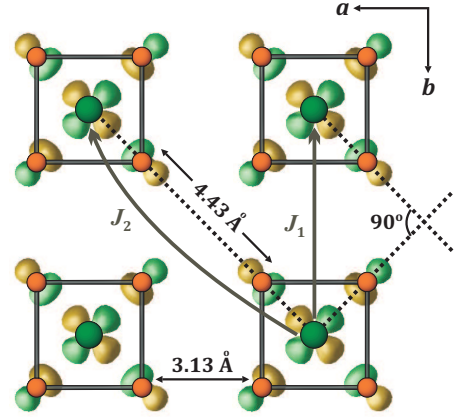


FIG. 7. (Color online) Cu $d_{x^2-y^2}$ -based Wannier functions, and the scheme of Cu–O...O–Cu superexchange pathways in diabolite. Different colors show different signs of the Wannier function. Larger (green) and smaller (orange) spheres denote the Cu and O atoms, respectively. The nearest-neighbor coupling J_1 features the 90° orbital overlap and shorter O...O distances (3.13 Å), whereas J_2 corresponds to the 180° overlap and longer O...O distance (4.43 Å).

and for the diabolite with $\frac{1}{4}$ of Cu vacancies (Fig. 3). The formation of vacancies does not disrupt the couplings between the remaining Cu sites: the intralayer hoppings t_1 are in the range 74 – 79 meV, which is very close to $t_1 = 78$ meV for the stoichiometric compound. The effect of stacking faults is also weak. However, the change in the stacking sequence should modify the regime of interlayer exchange by replacing J_{\perp} and J'_{\perp} with a single coupling J''_{\perp} , which is somewhat weaker than the interlayer couplings in the tetragonal structure (compare $t''_{\perp} \simeq 3$ meV with t_{\perp} and t'_{\perp} of ± 10 meV in Table I). The role of interlayer couplings in diabolite is further discussed in the next section.

D. Thermodynamic properties

Magnetic susceptibility of diabolite shows a maximum at $T^{\text{max}} \simeq 32$ K followed by a kink at $T_N = 11 - 12$ K (Fig. 8). This kink is somewhat field-dependent (Fig. 9) and indicates the onset of long-range magnetic order. Above 200 K, the susceptibility follows the Curie-Weiss law

$$\chi = \chi_0 + \frac{C}{T + \theta},$$

with $\chi_0 = -2 \times 10^{-4}$ emu/mol, $C = 0.512$ emu K/mol, and $\theta = 35$ K. The sizable temperature-independent diamagnetic contribution is likely related to the contribution of the sample holder and core diamagnetism. The C value yields the effective magnetic moment $\mu_{\text{eff}} = 2.02 \mu_B$, which is notably higher than $1.73 \mu_B$ expected for spin- $\frac{1}{2}$. The deviation of μ_{eff} from the spin-only value implies $g \simeq 2.32$, which is rather high but still in the reasonable range for Cu^{+2} compounds (see, e.g., Ref. 49). The

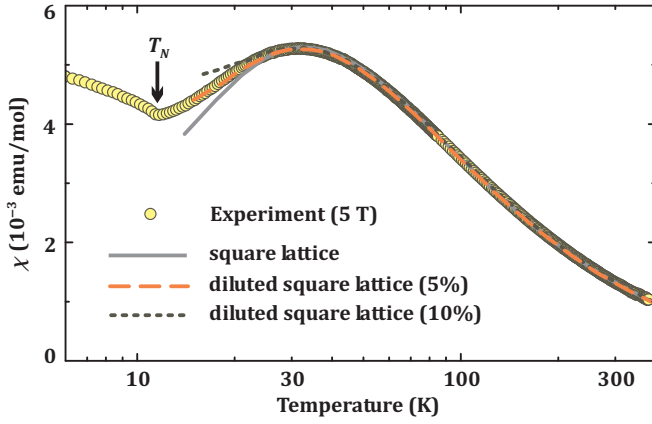


FIG. 8. (Color online) Magnetic susceptibility of diabolite measured in the applied field of 5 T (circles) and QMC fits of three spin models (lines): the stoichiometric square lattice and the square lattices with 5% and 10% of vacancies. The arrow denotes the Néel temperature $T_N \simeq 11.5$ K at 5 T.

positive θ value implies predominantly AFM exchange couplings.

The susceptibility maximum can be approximated by a QMC fit for the purely 2D Heisenberg model of the spin- $\frac{1}{2}$ square lattice (solid line in Fig. 8). We find $J = 35$ K, $g = 2.34$, and $\chi_0 = -2 \times 10^{-4}$ emu/mol in excellent agreement with the high-temperature Curie-Weiss fit. However, the square-lattice model fails to describe the data below the susceptibility maximum. In this region, the fit can be improved by considering a diluted square lattice with randomly distributed vacancies. The dilution of spin- $\frac{1}{2}$ sites with vacancies increases the susceptibility below T^{\max} and eventually blurs the maximum. We find the best fit for the lattice with 5 % of vacancies, $J = 37$ K, and nearly unchanged g and χ_0 parameters. This result perfectly matches $J_1 = 38$ K from DFT (Table I). The concentration of vacancies is well in line with the XRD data that yield about 6 % Cu deficiency (Sec. III A).

The shape of the susceptibility curve below T^{\max} is a strong evidence for the formation of vacancies in the magnetic layers of diabolite. Although 3D correlations (interplane couplings) might have similar effect on the susceptibility, their contribution is not strong enough to explain the experimental data. For example, weakly coupled square planes with an effective interlayer coupling $J_{\perp}^{\text{eff}}/J_1 = 6.5 \times 10^{-3}$, which reproduces the magnetic transition temperature in diabolite (see Fig. 10), show nearly the same susceptibility as the single square plane.

The antiferromagnetic ordering in diabolite manifests itself by a kink of the magnetic susceptibility (Fig. 9). The Néel temperature increases with the applied field. The magnetic transition is not well seen in zero-field specific heat, although a close examination of the C_p/T data at 11–12 K spots a tiny feature at 10.7 K (see the inset of Fig. 10). Otherwise, the temperature dependence of the zero-field specific heat is smooth up to at least 100 K.³⁹ A magnetic field enhances the transition anomaly that

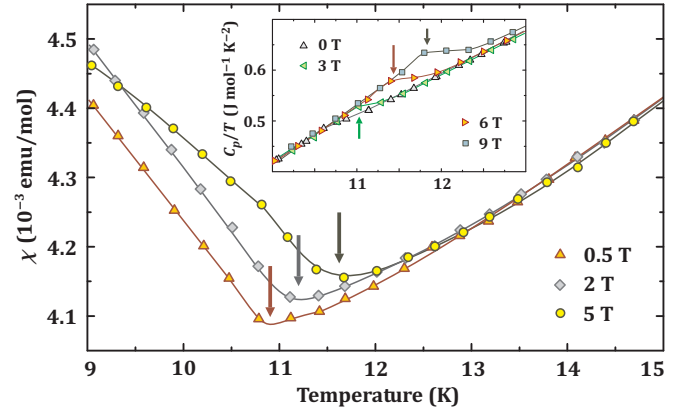


FIG. 9. (Color online) Field dependence of the Néel temperature in diabolite, as seen from the magnetic susceptibility and specific heat (inset) data. Lines are guide for the eye. Arrows denote the transition temperatures (see text for details).

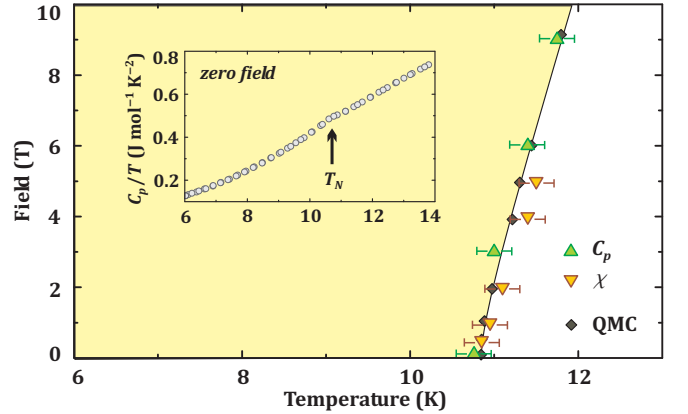


FIG. 10. (Color online) Field-temperature phase diagram derived from QMC simulations for weakly coupled square planes with an effective interlayer coupling $J_{\perp}^{\text{eff}}/J_1 = 6.5 \times 10^{-3}$. Experimental values of T_N are shown according to the magnetic susceptibility (χ) and specific heat (C_p) data. Left (colored) and right (white) parts are the magnetically ordered and paramagnetic phases, respectively. The inset shows the specific heat measured in zero field.

becomes well visible at 6 T and 9 T (see the inset of Fig. 9).

The broadening of the transition anomalies, which is inevitable in powder samples, prevents us from the precise evaluation of T_N in different magnetic fields. Nevertheless, the data in Fig. 9 show clearly that T_N increases with the applied field, and this trend holds up to at least 9 T. Using middle points of the local minima of the susceptibility, as well as the kinks in the specific heat data, we tentatively evaluate the field dependence of T_N (Fig. 10). The steady increase in T_N is very typical for spin- $\frac{1}{2}$ quantum magnets and resembles the field-induced behavior observed in other square-lattice systems with spin- $\frac{1}{2}$.^{13,37}

To analyze the field dependence of T_N , we first consider the magnetic transition in zero field. The 3D AFM order is driven by the interlayer couplings J_\perp and J'_\perp . These couplings are comparable in strength (see Table I) and frustrated, because they favor different interlayer spin configurations: G-type (antiparallel spins on nearest neighbors along c) and C-type (parallel spins on nearest neighbors along c), respectively. However, the DFT evaluation of J_\perp and J'_\perp comes with a caveat that the couplings on the order of 1 K are very difficult to estimate precisely, and a careful experimental work, such as inelastic neutron scattering at very low energies, would be necessary to get accurate values of J_\perp and J'_\perp . Here, we argue that the experimental data are in agreement with an effective non-frustrated interlayer exchange that might be a combination of J_\perp and J'_\perp .

We have studied the AFM ordering in weakly coupled square planes by QMC simulations of a 3D spin model with the uniform interlayer coupling J_\perp^{eff} (see Refs. 37 and 50 for similar studies). The J_\perp^{eff} parameter was adjusted as to match $T_N \simeq 10.7$ K in zero field. The resulting estimate of $J_\perp^{\text{eff}}/J_1 = 6.5 \times 10^{-3}$ (i.e., $J_\perp^{\text{eff}} \simeq 0.2$ K) is somewhat smaller than J_\perp and J'_\perp (Table I) and may reflect their partial compensation. Using this value of J_\perp^{eff} , we are able to reproduce both T_N in zero field and the field dependence of T_N (Fig. 10). This way, the experimental data available so far are in agreement with the spin model of weakly coupled square planes without any substantial frustration. Regarding the role of Cu vacancies and stacking faults, their effect on the interlayer exchange is likely minor and can not be distinguished using the experimental data available so far.

The physical mechanism behind the increase in T_N is the suppression of quantum fluctuations by the applied magnetic field. In higher fields, this effect is countered by the increasing tendency toward parallel spin arrangement (see, e.g., Ref. 37). However, the AFM couplings in diabolite are strong enough to compete with the field, so that the T_N increases linearly up to at least 9 T.

IV. DISCUSSION AND SUMMARY

Our study of diabolite raises several problems that may have implications for other quantum magnets and for theoretical models of quantum magnetism. First, our anticipation of the sizable second-neighbor coupling J_2 was not confirmed in the experimental and computational study. While diabolite indeed bears structural similarity to PbVO_3 , which is the strongly frustrated square-lattice compound with sizable J_2 ,²⁰ details of their electronic structures are notably different. In PbVO_3 , vanadium polyhedra are directly connected to each other, thus leading to relatively short pathways for J_1 (V–V distance of 3.88 Å) and J_2 (5.49 Å). The diabolite structure features isolated CuO_4 plaquettes, hence both J_1 and J_2 correspond to much longer Cu–Cu distances of 5.88 Å and 8.32 Å, respectively.

The substantial elongation of the metal–metal distances in diabolite could be mitigated by a different symmetry of the magnetic $3d$ orbital. In contrast to the half-filled d_{xy} orbital of V^{4+} , the $d_{x^2-y^2}$ orbital of Cu^{+2} features the strong σ -overlap with the oxygen p orbitals. This way, the Wannier functions are extended by large oxygen contributions (“tails”) that can overlap and eventually lead to strong couplings even for very long superexchange pathways. In diabolite, this mechanism is indeed operative for J_1 , where the O–O distance of 3.13 Å results in a sizable coupling of 35 K despite the 90° overlap, which is generally deemed unfavorable for the AFM coupling. Regarding J_2 , the O–O distance of 4.43 Å appears to be too long for any appreciable magnetic interaction, even though the orbitals form the favorable 180° geometry (Fig. 7).

The second interesting aspect of the diabolite magnetism pertains to experimental signatures of the magnetic transition. While the susceptibility measurements unequivocally demonstrate the 3D magnetic ordering below $T_N \simeq 11$ K (Fig. 9), heat capacity measured in zero magnetic field shows only a tiny feature that, when examined on its own, may be well considered an artifact (see the inset of Fig. 10). The lack of a conspicuous transition anomaly is caused by the small amount of the magnetic entropy available at T_N . Using QMC simulations, we estimate that in zero field only 7 % of the magnetic entropy can be released at T_N . The main release of the entropy is observed at $T \simeq J$ as a broad maximum in the temperature dependence of the magnetic specific heat.^{51,52} An external magnetic field shifts the entropy from the broad maximum at $T \simeq J$ toward the transition anomaly at T_N .¹³ This way, the transition anomaly becomes visible and can be tracked with heat-capacity measurements.

Similar effects of low magnetic entropy at T_N and its dramatic increase in the applied field have been reported for the square-lattice magnets with weak exchange couplings and relatively low saturation fields.^{13,16} Although diabolite features the stronger exchange and the high saturation field (expected at $H_s = 4J_1/g\mu_B \simeq 120$ T), even the low fields of 6–9 T ($H/H_s = 0.05 - 0.075$) are sufficient to render the transition anomaly visible. Our experimental results are in line with earlier reports on other spin- $\frac{1}{2}$ materials. For example, Lancaster *et al.*¹⁴ claimed that quasi-2D systems with weak interlayer exchange do not show transition anomalies in the specific heat, whereas Sengupta *et al.*⁵¹ demonstrated the suppression of the transition anomaly depending on the size of the interlayer couplings. Our data emphasize the importance of heat-capacity measurements in high magnetic fields, because an external field enhances the anomaly and facilitates an experimental observation of the magnetic transitions. This result may be relevant to the controversial magnetic transition in PbVO_3 as well.^{19,20}

Diabolite is a rare material showing magnetism of the diluted square lattice with spin- $\frac{1}{2}$. We have proved the formation of Cu vacancies by XRD and chemical analy-

sis, and observed the dilution effect in magnetic susceptibility measurements (Fig. 8). If the concentration of Cu vacancies could be varied (e.g., by crystal growth in Cu-deficient environment), diabolite becomes an interesting system with a remarkably “clean” mechanism of dilution. Presently, most studies of the diluted square lattice focus on Zn- and Mg-doped La_2CuO_4 , where the doping with non-magnetic atoms leads to a frustration of the spin lattice by the second-neighbor coupling J_2 .^{53,54} In diabolite, this effect is suppressed, because the Cu–Cu distances are very large and prevent any long-range superexchange interactions (Fig. 7). The diluted spin- $\frac{1}{2}$ systems provide a unique opportunity to study the interplay of disorder and quantum fluctuations.^{54–57} Therefore, further studies of diabolite may be insightful.

More generally, an in-depth physics research performed on natural samples is a delicate compromise between the potential complexity of the sample and the tantalizing opportunity to find unexpected structural and physical effects. Natural samples are prone to contamination by foreign phases and elements. A meticulous sample characterization is an essential part of the work that often ends when the sample is found unsuitable, owing to a contamination by magnetic impurities. However, sample imperfections can be advantageous as well. Sometimes they disclose interesting effects that are neither expected nor observed in synthetic samples. We hope that the study of Cu-based minerals will further contribute to the experimental and theoretical work on quantum magnetism. Detailed characterization of the chemical composition, crystal structure, and physical properties should also advance our understanding of intricate natural processes that lead to the formation of these interesting and

aesthetically beautiful materials.

In summary, we have studied the crystal structure and magnetism of the diabolite mineral. The formation of Cu vacancies, which are tolerated by the crystal structure, leads to the dilution of the spin lattice. This effect is probed directly via chemical analysis and XRD, as well as indirectly via magnetic susceptibility measurements that show clear signatures of the dilution. The concentration of vacancies is about 5%. Consistently, thermodynamic properties of diabolite are well described by the spin model of the diluted square lattice with the nearest-neighbor exchange $J_1 \simeq 37$ K and 5% of Cu vacancies. Weak interlayer couplings trigger the long-range magnetic order below $T_N \simeq 10.7$ K in zero field.

ACKNOWLEDGMENTS

We are grateful to Gudrun Auffermann for her kind help with the chemical analysis of small mineral samples. We also acknowledge the experimental support by Walter Schnelle and Deepa Kasinathan (thermodynamic measurements), Yurii Prots and Horst Borrmann (laboratory XRD), Yves Watier (ID31), and the provision of the ID31 beamtime by ESRF. We would like to thank the Department of Materials Research and Physics of the Salzburg University for providing the high-quality natural sample of diabolite from their mineralogical collection (inventory number 2536). AT was supported by the Mobilitas program of the ESF. SL acknowledges the funding from the Austrian Fonds zur Förderung der wissenschaftlichen Forschung (FWF) via a Schrödinger fellowship J3247-N16.

* altsirlin@gmail.com

† Helge.Rosner@cpfs.mpg.de

¹ M. B. Stone, I. A. Zaliznyak, T. Hong, C. L. Broholm, and D. H. Reich, *Nature* **440**, 187 (2006).

² T. Giamarchi, C. Rüegg, and O. Tchernyshyov, *Nature Physics* **4**, 198 (2008).

³ L. Balents, *Nature* **464**, 199 (2010).

⁴ S. Seki, X. Z. Yu, S. Ishiwata, and Y. Tokura, *Science* **336**, 198 (2012).

⁵ F. Kagawa, S. Horiuchi, M. Tokunaga, J. Fujioka, and Y. Tokura, *Nature Phys.* **6**, 169 (2010).

⁶ B. Wolf, Y. Tsui, D. Jaiswal-Nagar, U. Tutsch, A. Honecker, K. Remović-Langer, G. Hofmann, A. Prokofiev, W. Assmus, G. Donath, and M. Lang, *Proc. Nat. Acad. Sci.* **108**, 6862 (2011).

⁷ G. Misguich and C. Lhuillier, in *Frustrated spin systems*, edited by H. T. Diep (World Scientific, Singapore, 2004) and references therein.

⁸ N. Shannon, B. Schmidt, K. Penc, and P. Thalmeier, *Eur. Phys. J. B* **38**, 599 (2004).

⁹ R. Darradi, O. Derzhko, R. Zinke, J. Schulenburg, S. E. Krüger, and J. Richter, *Phys. Rev. B* **78**, 214415 (2008).

¹⁰ J. Richter, R. Darradi, J. Schulenburg, D. J. J. Farnell, and H. Rosner, *Phys. Rev. B* **81**, 174429 (2010).

¹¹ H.-C. Jiang, H. Yao, and L. Balents, *Phys. Rev. B* **86**, 024424 (2012).

¹² E. Kaul, H. Rosner, N. Shannon, R. Shpanchenko, and C. Geibel, *J. Magn. Magn. Mater.* **272–276**, 922 (2004); A. A. Tsirlin, B. Schmidt, Y. Skourski, R. Nath, C. Geibel, and H. Rosner, *Phys. Rev. B* **80**, 132407 (2009), and references therein.

¹³ R. Nath, A. A. Tsirlin, H. Rosner, and C. Geibel, *Phys. Rev. B* **78**, 064422 (2008); A. A. Tsirlin, R. Nath, A. M. Abakumov, Y. Furukawa, D. C. Johnston, M. Hemmida, H.-A. Krug von Nidda, A. Loidl, C. Geibel, and H. Rosner, *ibid.* **84**, 014429 (2011).

¹⁴ T. Lancaster, S. J. Blundell, M. L. Brooks, P. J. Baker, F. L. Pratt, J. L. Manson, M. M. Conner, F. Xiao, C. P. Landee, F. A. Chaves, S. Soriano, M. A. Novak, T. P. Papageorgiou, A. D. Bianchi, T. Herrmannsdörfer, J. Wosnitza, and J. A. Schlueter, *Phys. Rev. B* **75**, 094421 (2007); P. A. Goddard, J. Singleton, P. Sengupta, R. D. McDonald, T. Lancaster, S. J. Blundell, F. L. Pratt, S. Cox, N. Harrison, J. L. Manson, H. I. Southerland, and J. A. Schlueter, *New. J. Phys.* **10**, 083025 (2008).

- ¹⁵ N. Tsyrlin, T. Pardini, R. R. P. Singh, F. Xiao, P. Link, A. Schneidewind, A. Hiess, C. P. Landee, M. M. Turnbull, and M. Kenzelmann, *Phys. Rev. Lett.* **102**, 197201 (2009).
- ¹⁶ N. Tsyrlin, F. Xiao, A. Schneidewind, P. Link, H. M. Rønnow, J. Gavilano, C. P. Landee, M. M. Turnbull, and M. Kenzelmann, *Phys. Rev. B* **81**, 134409 (2010).
- ¹⁷ M. Siahhatgar, B. Schmidt, and P. Thalmeier, *Phys. Rev. B* **84**, 064431 (2011).
- ¹⁸ P. Carretta, N. Papinutto, C. B. Azzoni, M. C. Mozzati, E. Pavarini, S. Gonthier, and P. Millet, *Phys. Rev. B* **66**, 094420 (2002); A. Bombardi, L. C. Chapon, I. Margiolaki, C. Mazzoli, S. Gonthier, F. Duc, and P. G. Radaelli, *ibid.* **71**, 220406(R) (2005).
- ¹⁹ K. Oka, I. Yamada, M. Azuma, S. Takeshita, K. H. Satoh, A. Koda, R. Kadono, M. Takano, and Y. Shimakawa, *Inorg. Chem.* **47**, 7355 (2008).
- ²⁰ A. A. Tsirlin, A. A. Belik, R. V. Shpanchenko, E. V. Antipov, E. Takayama-Muromachi, and H. Rosner, *Phys. Rev. B* **77**, 092402 (2008).
- ²¹ A. Belik, S. Iikubo, K. Kodama, N. Igawa, S. Shamoto, S. Niitaka, M. Azuma, Y. Shimakawa, M. Takano, F. Izumi, and E. Takayama-Muromachi, *Chem. Mater.* **18**, 798 (2006).
- ²² For example: H. Béa, B. Dupé, S. Fusil, R. Mattana, E. Jacquet, B. Warot-Fonrose, F. Wilhelm, A. Rogalev, S. Petit, V. Cros, A. Anane, F. Petroff, K. Bouzehouane, G. Geneste, B. Dkhil, S. Lisenkov, I. Ponomareva, L. Bellaiche, M. Bibes, and A. Barthélémy, *Phys. Rev. Lett.* **102**, 217603 (2009).
- ²³ R. C. Rouse, *Z. Kristallogr.* **134**, 69 (1971).
- ²⁴ M. A. Cooper and F. C. Hawthorne, *Can. Miner.* **33**, 1125 (1995).
- ²⁵ ICP-OES (inductively coupled plasma optical emission spectrometry) analysis was performed with the VISTA instrument from Varian.
- ²⁶ V. Petříček, M. Dušek, and L. Palatinus, “Jana2006. The crystallographic computing system,” (2006), Institute of Physics, Praha, Czech Republic.
- ²⁷ K. Momma and F. Izumi, *J. Appl. Crystallogr.* **44**, 1272 (2011).
- ²⁸ K. Koepnick and H. Eschrig, *Phys. Rev. B* **59**, 1743 (1999).
- ²⁹ G. Kresse and J. Furthmüller, *Comput. Mater. Sci.* **6**, 15 (1996); *Phys. Rev. B* **54**, 11169 (1996).
- ³⁰ P. E. Blöchl, *Phys. Rev. B* **50**, 17953 (1994); G. Kresse and D. Joubert, *ibid.* **59**, 1758 (1999).
- ³¹ J. P. Perdew and Y. Wang, *Phys. Rev. B* **45**, 13244 (1992).
- ³² J. P. Perdew, K. Burke, and M. Ernzerhof, *Phys. Rev. Lett.* **77**, 3865 (1996).
- ³³ For example: S. Lebernegg, A. A. Tsirlin, O. Janson, R. Nath, J. Sichelschmidt, Y. Skourski, G. Amthauer, and H. Rosner, *Phys. Rev. B* **84**, 174436 (2011); A. A. Tsirlin, A. Möller, B. Lorenz, Y. Skourski, and H. Rosner, *ibid.* **85**, 014401 (2012).
- ³⁴ S. Todo and K. Kato, *Phys. Rev. Lett.* **87**, 047203 (2001).
- ³⁵ F. Alet, S. Wessel, and M. Troyer, *Phys. Rev. E* **71**, 036706 (2005), and references therein.
- ³⁶ A. Albuquerque, F. Alet, P. Corboz, P. Dayal, A. Feiguin, S. Fuchs, L. Gamper, E. Gull, S. Gürtler, A. Honecker, R. Igarashi, M. Körner, A. Kozhevnikov, A. Läuchli, S. Manmana, M. Matsumoto, I. McCulloch, F. Michel, R. Noack, G. Pawłowski, L. Pollet, T. Pruschke, U. Schollwöck, S. Todo, S. Trebst, M. Troyer, P. Werner, and S. Wessel, *J. Magn. Magn. Mater.* **310**, 1187 (2007).
- ³⁷ P. Sengupta, C. D. Batista, R. D. McDonald, S. Cox, J. Singleton, L. Huang, T. P. Papageorgiou, O. Ignatchik, T. Herrmannsdörfer, J. L. Manson, J. A. Schlueter, K. A. Funk, and J. Wosnitzer, *Phys. Rev. B* **79**, 060409(R) (2009).
- ³⁸ A. A. Tsirlin and H. Rosner, *Phys. Rev. B* **83**, 064415 (2011); A. A. Tsirlin, A. M. Abakumov, C. Ritter, and H. Rosner, *ibid.* **86**, 064440 (2012).
- ³⁹ See Supplemental Material for details of the Rietveld refinement, refined atomic positions, and zero-field heat capacity of diabolite.
- ⁴⁰ Edge-sharing CuO_4 plaquettes in the crystal structure of wherryite suggest similarities to linarite $[\text{PbCu}(\text{OH})_2\text{SO}_4]$, Li_2CuO_2 , and other $J_1 - J_2$ chain antiferromagnets: see, e.g., Ref. 49.
- ⁴¹ Note that the ADP and occupancy factor have similar effect on the scattering density and can not be refined simultaneously.
- ⁴² Note that we do not use DFT+ U because Hubbard-type electronic correlations introduced in this approach are only relevant to the Cu site, which is kept fixed in the relaxation.
- ⁴³ A. M. Abakumov, D. Batuk, J. Hadermann, M. G. Rozova, D. V. Sheptyakov, A. A. Tsirlin, D. Niermann, F. Waschowski, J. Hemberger, G. Van Tendeloo, and E. V. Antipov, *Chem. Mater.* **23**, 255 (2011).
- ⁴⁴ S. Åsbrink and L.-J. Norrby, *Acta Cryst.* **B26**, 8 (1970).
- ⁴⁵ R. E. Winchell and H. E. Wenden, *Mineralogical Magazine* **36**, 933 (1968).
- ⁴⁶ C. B. Aakeröy, T. A. Evans, K. R. Seddon, and I. Pálinkó, *New J. Chem.* **23**, 145 (1999); T. Steiner, *Angew. Chem. Int. Ed.* **41**, 48 (2002).
- ⁴⁷ The sizable hopping t'_\perp leads to a deceptive picture in the tight-binding analysis. Normally, one uses the energies at the Γ , X , and M points for a preliminary evaluation of t_2/t_1 . For $t_2 = 0$, $\varepsilon_\Gamma - \varepsilon_X = \varepsilon_X - \varepsilon_M$, which is not the case for diabolite (i.e., a sizable t_2 should be expected). However, the deviation from the simple t_1 square lattice is due to both t_2 and t'_\perp that are indistinguishable in the ab plane of the reciprocal space ($\Gamma - X - M$). The hopping t'_\perp connects each Cu site to 8 neighbors and has strong effect on the dispersion, whereas t_2 is small.
- ⁴⁸ See, for example: P. W. Anderson, *Solid State Physics* **14**, 99 (1963); V. V. Mazurenko, S. L. Skorniyakov, A. V. Kozhevnikov, F. Mila, and V. I. Anisimov, *Phys. Rev. B* **75**, 224408 (2007).
- ⁴⁹ S. Zvyagin, G. Cao, Y. Xin, S. McCall, T. Caldwell, W. Moulton, L.-C. Brunel, A. Angerhofer, and J. E. Crow, *Phys. Rev. B* **66**, 064424 (2002); A. U. B. Wolter, F. Lipps, M. Schäpers, S.-L. Drechsler, S. Nishimoto, R. Vogel, V. Kataev, B. Büchner, H. Rosner, M. Schmitt, M. Uhlir, Y. Skourski, J. Wosnitzer, S. Süllo, and K. C. Rule, *ibid.* **85**, 014407 (2012).
- ⁵⁰ C. Yasuda, S. Todo, K. Hukushima, F. Alet, M. Keller, M. Troyer, and H. Takayama, *Phys. Rev. Lett.* **94**, 217201 (2005).
- ⁵¹ P. Sengupta, A. W. Sandvik, and R. R. P. Singh, *Phys. Rev. B* **68**, 094423 (2003).
- ⁵² M. S. Makivić and H.-Q. Ding, *Phys. Rev. B* **43**, 3562 (1991).
- ⁵³ For example: C.-W. Liu, S. Liu, Y.-J. Kao, A. L. Chernyshev, and A. W. Sandvik, *Phys. Rev. Lett.* **102**, 167201 (2009); P. Carretta, G. Prando, S. Sanna, R. De Renzi, C. Decorse, and P. Berthet, *Phys. Rev. B* **83**, 180411(R) (2011).

- ⁵⁴ J.-Y. P. Delannoy, A. G. Del Maestro, M. J. P. Gingras, and P. C. W. Holdsworth, Phys. Rev. B **79**, 224414 (2009).
⁵⁵ O. P. Vajk, P. K. Mang, M. Greven, P. M. Gehring, and J. W. Lynn, Science **295**, 1691 (2002).

- ⁵⁶ A. L. Chernyshev, Y. C. Chen, and A. H. Castro Neto, Phys. Rev. Lett. **87**, 067209 (2001); Phys. Rev. B **65**, 104407 (2002).
⁵⁷ K. H. Höglund and A. W. Sandvik, Phys. Rev. Lett. **91**, 077204 (2003).

Supplementary information for
Square-lattice magnetism of diabolite $\text{Pb}_2\text{Cu}(\text{OH})_4\text{Cl}_2$

A. A. Tsirlin, O. Janson, S. Lebernegg, and H. Rosner

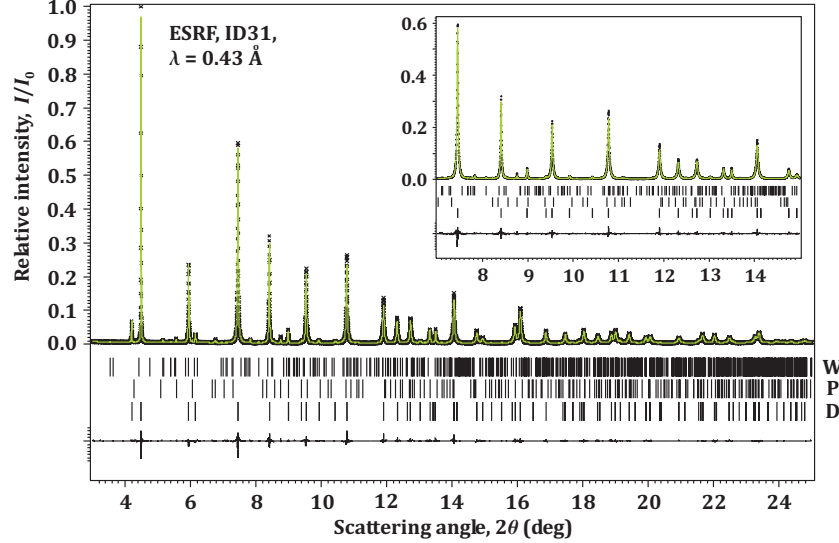


FIG. 11. Rietveld refinement of the room-temperature high-resolution XRD data. Ticks show the reflection positions, from bottom to top: diabolite (D), phosgenite (P), and wherryite (W). Note that for the diabolite phase we had to refine the anisotropic strain broadening parameters S_{hkl} (in $10^{-2} \text{ deg}^2 \text{ Å}^{-4}$): $S_{400} = S_{004} = -0.033(2)$, $S_{220} = 0.119(3)$, $S_{202} = S_{022} = 0.162(3)$, $S_{004} = 0$. The definition of S_{hkl} is according to the Jana2006 program, see also [P. W. Stephens, J. Appl. Cryst. 32, 281 (1999)].

TABLE II. Atomic positions, atomic displacements parameters U_{iso} (in 10^{-2} Å^2), and occupation factors g refined from the powder data on the natural sample of diabolite. Although the accuracy of the structural parameters is probably lower than in [M. A. Cooper and F. C. Hawthorne, Canad. Mineralog. 33, 1125 (1995)], where single-crystal data were used, our refinement provides information on peculiarities of the particular sample used in the present work. Error bars are obtained from the Rietveld refinement.

Atom	Wyckoff position	x/a	y/b	z/c	U_{iso}	g
Pb	$2c$	0	$\frac{1}{2}$	0.7298^a	$1.2(1)$	1.0
Cu	$1a$	0	0	$0.008(3)$	1.0^b	$0.942(4)$
Cl1	$1a$	0	0	$0.464(3)$	$0.1(1)^c$	1.0
Cl2	$1b$	$\frac{1}{2}$	$\frac{1}{2}$	$0.404(2)$	$0.1(1)^c$	1.0
O	$4d$	$0.2452(6)$	$0.2452(6)$	$0.9654(8)$	$1.3(1)$	1.0
H ^d	$4d$	0.291	0.291	0.122	1.0	1.0

^a The z coordinate of the Pb atom is fixed in order to keep the position of origin

^b Only the occupancy factor was refined

^c The atomic displacements parameters of Cl1 and Cl2 were refined as a single parameter

^d The position of hydrogen was not refined

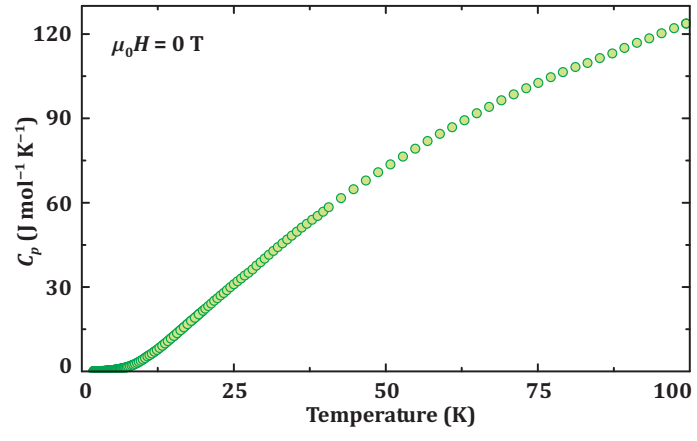


FIG. 12. Zero-field heat capacity of diabolite.